CANADIAN TRANSACTIONS OF MATHEMATICAL COMPUTING
Volume 1, Issue 1, (2025) Article 250104

HEAT AND MASS TRANSFER WITHIN MHD WILLIAMSON NANOFLUID FLOW UNDER VELOCITY AND THERMAL SLIPS IN POROUS MEDIUM: NUMERICAL AND SEMI-NUMERICAL APPROACH

VISHWANATH AWATI[1*], SACHIN MUCHANDI[2], MAHESH KUMAR N[3] AND AKASH GORAVAR[4]

[1,2,3] *Department of Mathematics, Rani Channamma University, Belagavi-591156, India*
[4] *Department of Mathematics and Statistics, Ramaiah University of Applied Sciences, Bangalore-560058, India*

Email: [1] *awati.vb@rcub.ac.in,*
[2] *sachinmuchandi456@gmail.com,*[3] *maheshkumarnmk98@gmail.com,*[4] *akashgoravar.mt.ns@msruas.ac.in*

ABSTRACT. The paper presents numerical and semi-numerical simulations of a double diffusive magnetohydrodynamic boundary layer flow of Williamson nanofluid over a linear stretching surface. The analysis incorporates the combined effects of velocity and thermal slips, porosity, chemical reaction, diffusivity ratio, heat capacity ratio and internal heat source/sink. Using suitable similarity variables the leading partial differential equations are transformed into a self-similar system of coupled nonlinear ordinary differential equations. These equations are solved using the robust Keller box and Haar wavelet collocation methods. Both methods exhibited excellent numerical symmetry with each other as well as the prevailing literature. The influence of involved thermophysical parameters on velocity, temperature and concentration fields is presented through tables and graphs. This analysis reveals that boundary layer thickness reduces due to the rise in slip parameters, while higher Williamson parameter enhances both temperature and concentration profiles, accompanied by a reduction in the skin friction coefficient.

2020 Mathematics Subject Classification: 34D20, 92D40, 93A30
Keywords. Williamson Nanofluid, MHD Flow, Slip Conditions, Keller-box Method, Haar Wavelet Collocation Method.

1. INTRODUCTION

The study of nanofluids holds immense potential for modern thermal optimization techniques to enhance the heat transfer efficiency in various fields, ranging from electronics to renewable energy. The study of nanofluids was initiated by Choi [1] and Eastman et al. [2]. Nanofluids are the engineered colloidal suspensions of 1-100 nm nanosized (Taylor et al. [3]) metallic particles of aluminium, copper, iron, gold or their oxides etc. in a base fluid such as oil, water, toluene, or ethylene glycol to improve thermophysical properties of the conventional base fluid. Choi [1] conceived that the addition of nanoparticles to the conventional liquids increases their thermal conductivity. Further, Eastman et al. [2] acheived a twofold heat transfer efficiency by adding less than 1% of nanoparticles to the base fluid. Buongiorno [4] revealed that Brownian diffusion and thermophoresis stand as the significant slip mechanisms. Among the seven available mechanisms, it is capable of inducing relative velocity between nanoparticles and base fluid. Corcione et al. [5] studied nanofluid natural convection within a differentially heated enclosure using Buongiorno's model and observed dual-phase mixture approach outperformed the single-phase model in accuracy. Rana and Bhargava [6] demonstrated the nanofluid

Received: August 2025, Accepted: December 2025.
* Corresponding author.

model by elaborating the consequences of thermophoresis and Brownian motion on nanofluids. Xuan and Li [7] discussed convective heat and mass transfer characteristics of nanofluids. The non-Newtonian nanofluids adapt their viscosity based on external forces rather than adhering to standard fluid dynamics principles. Their unique ability to shift from fluid to solid-like states in response to stress has led to diverse applications (Wong and Leon [8]) in various industries such as food industry, metal extrusion, glass manufacture, and crude oil purification, etc. Krishnamurthy et al. [9] classified Williamson nanofluid as a visco-inelastic fluid. The core advantage of Williamson nanofluid stems from its ability to significantly enhance thermal conductivity and heat transfer efficiency in comparison to the base fluid alone. This improvement is attributed to the nanoparticles' high surface area to volume ratio which facilitates more effective heat transfer between the fluid and its surroundings.

The boundary layer flow problem on a flat plate was studied by Blasius [10] through similarity transformation. Ramesh et al. [11] investigated convective boundary conditions in Sakiadis and Blasius flows of a Williamson fluid. Awati et al. [12] discussed heat and mass transfer features of nanofluid over a nonlinear stretching sheet using the Haar wavelet collocation method (HWCM). Further, Awati and Mahesh [13] extended the work of [12] to a semi-infinite static and moving flat plate. Liao [14] examined the boundary layer flow problem over an impermeable stretching sheet using the Homotopy analysis method (HAM). Khan and Khan [15] investigated boundary layer flows of a non-Newtonian Williamson fluid using HAM and concluded that boundary layer thickness is inversely proportional to the Williamson parameter. Crane [16] derived the exact analytical solution of boundary layer flow over a stretching plate. Magneto-hydrodynamics (MHD) plays a vital role in controlling the fluid flow and heat transfer by applying a magnetic field to electrically conducting fluids. Ishak et al. [17] extended the work of [16] and studied heat transfer through MHD flow over a vertically stretched sheet. Nadeem and Hussain [18] scrutinized MHD effects on Williamson nanofluid flow over a heated surface. Kumar et al. [19] examined the three-dimensional MHD flow of chemically reactive Williamson fluid by considering non-uniform heat absorption and generation.

The transfer of heat energy occurs due to the temperature difference between connected objects. The rate of heat transfer as well as prevention of thermal loss, has become a common and important aspect in various fields like electronic packaging, reactor cooling systems etc. Grubka et al. [20] explored the heat transfer characteristics with variable temperature on a uniform stretching surface. Later, Chen [21] presented the effect of Prandtl number and buoyancy force on the heat and mass transfer over a continuously stretching vertical sheet. Rosali et al. [22] demonstrated the micropolar fluid flow in a porous medium towards a permeable stretching/shrinking sheet. Hayat et al. [23] studied the MHD flow and heat transfer on a permeable stretching surface with slip condition. Yasin et al. [24] continued the work of [22] with the radiation effect. Nazir et al. [25] studied the non-Fourier heat and mass transfer through chemically reactive hybrid Williamson nanofluid with Forchheimer porous medium. Further, Awati and Goravar [26] semi-numerically investigated chemically reactive MHD nanofluid flow over a non-isothermal porous medium. Awati et al. [27] scrutinized the Chebyshev collocation method for mass transfer over a continuously moving flat plate in the presence of chemical reaction.

The governing equations of non-Newtonian fluid flows are generally nonlinear and finding their analytical solution is quite challenging. Among various numerical and semi-numerical schemes, the Keller box method (KBM) and the Haar wavelet collocation method (HWCM) are robust techniques to solve such problems. Ramya et al. [28] illustrated the heat and mass transfer of viscous nanofluids with thermal wall slip effect using the KBM [29]. Bilal et al. [30] numerically explored the thermal stratified flow of Williamson fluid over a cylindrical surface via KBM. In recent years, wavelet techniques have been extensively used to solve complex linear and nonlinear differential equations. The wavelet method was first introduced by Haar [31]. Further, Grossman and Morlet [32] scrutinized the wavelet functions and their mathematical properties. Chen and Hsiao [33] derived the Haar wavelet operational matrices to obtain the solution of differential equation. In continuation of [33], Lepik [34, 35] presented the solution with uniform and non-uniform grid respectively. Awati et al. [36] demonstrated the spectral and Haar wavelet collocation methods to obtain the solution of MHD micropolar nanofluid flow with

the effects of heat generation and viscous dissipation. Recently, Awati et al. [37] investigated two-phase MHD nanofluid flow over a stretching permeable sheet of varible thickness using both KBM and HWCM.

The above literature review highlights the Williamson nanofluid flow over stretching surface have been studied extensively. The comparative numerical simulation using Keller box and Haar wavelet collocation methods for transport problem of Williamson nanofluid has not yet been adequately reported. This paper addresses the gap by investigating the heat and mass transfer characteristics of a double diffusive Williamson nanofluid flow over a porous stretching sheet with variable wall temperature. The novelty of the present work is further strengthened by incorporating the combined effects of velocity slip, thermal slip, Brownian motion, thermophoresis, chemical reaction, heat generation/absorption and transverse magnetic field. The self-similar ordinary differential equations (ODEs) are solved by using Keller box and Haar wavelet collocation methods. The analysis reveals that, physical parameters have a notable impact on fluid flow. It is expected that, outcomes of this paper not only complement with the existing research but also provides valuable perspectives for industrial applications. The paper is organized as follows: Section 2 presents mathematical formulation, methods of solution in Section 3, result and discussion in section 4 and conclusion in section 5.

2. Mathematical Formulation

Consider a steady state, incompressible flow of a two-dimensional Williamson nanofluid over a stretching surface. Let $U_w(x) = bx$ is the linear velocity on stretching sheet ($b > 0$) where x represent the co-ordinate measured along the elongating surface. Let y denotes the co-ordinate measured normal to the stretching sheet at $x = 0$. The physical model is depicted in Figure 1. C_w is uniformly distributed constant nanoparticle volume fraction and $T_w = T_\infty + ax^2$ is a variable wall temperature at the stretching surface with constant a. T_∞ and C_∞ denotes the ambient temperature and nanoparticle volume fraction far away from the sheet.

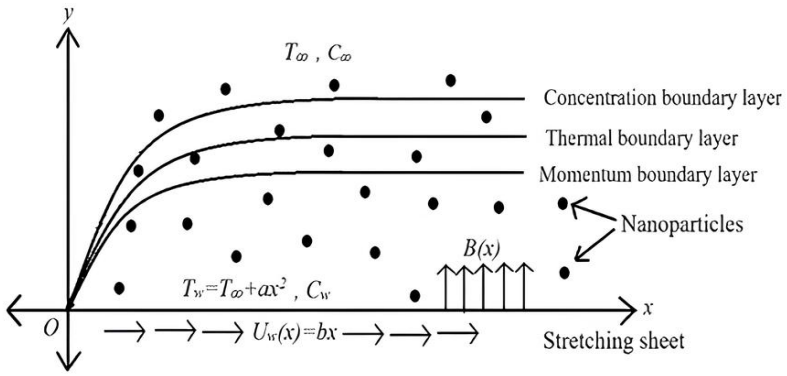

Figure 1. Geometrical representation of the flow

The leading equations for two-dimensional boundary layer flow of non-Newtonian Williamson nanofluid can be expressed as Kho et al. [39]

$$\frac{\partial u}{\partial x} + \frac{\partial v}{\partial y} = 0, \tag{1}$$

$$u\frac{\partial u}{\partial x} + v\frac{\partial u}{\partial y} = \nu\left[\frac{\partial^2 u}{\partial y^2} + \sqrt{2}\Gamma\frac{\partial u}{\partial y}\frac{\partial^2 u}{\partial y^2}\right] - \frac{\sigma B_0^2 u}{\rho} - \frac{\nu u}{K}, \tag{2}$$

$$u\frac{\partial T}{\partial x} + v\frac{\partial T}{\partial y} = \alpha\frac{\partial^2 T}{\partial y^2} + \frac{\rho_p C_p}{\rho C}\left[D_B\frac{\partial C}{\partial y}\frac{\partial T}{\partial y} + \frac{D_T}{T_\infty}\left(\frac{\partial T}{\partial y}\right)^2\right] + \frac{Q(T - T_\infty)}{\rho C}, \tag{3}$$

$$u\frac{\partial C}{\partial x} + v\frac{\partial C}{\partial y} = D_B\frac{\partial^2 C}{\partial y^2} + \frac{D_T}{T_\infty}\frac{\partial^2 T}{\partial y^2} - R(C - C_\infty). \tag{4}$$

The appropriate boundary conditions for the physical problem becomes

$$u = U_w + \xi^* \mu \frac{\partial u}{\partial y}, \quad v = 0, \quad T = T_w + \beta^* \frac{\partial T}{\partial y}, \quad C = C_w \quad \text{at} \quad y = 0, \tag{5}$$

$$u \to 0, \quad T \to T_\infty, \quad C \to C_\infty \quad \text{as} \quad y \to \infty, \tag{6}$$

where (u, v) are the respective velocity components of fluid along x and y directions. Let T denotes temperature and C is the nanoparticle volume fraction. ρ is the density of nanofluid, μ denotes the dynamic viscosity and ν represents kinematic viscosity of the nanofluid. Further, Γ, B_0, σ, K, α, D_B, D_T, Q and R respectively denotes the time constant, magnetic field constant, electrical conductivity, permeability of porous medium, thermal diffusivity, Brownian diffusion coefficient, thermophoresis diffusion coefficient, heat source/sink parameter and chemical reaction parameter.Physically, $Q > 0$ shows the heat generation whereas $Q < 0$ means the heat absorption. Also, $(\rho C)_p$ is the heat capacity of nanoparticle material and ρC is the heat capacity of the base fluid. ξ^* and β^* are the velocity and thermal slip parameters respectively.

The suitable similarity transformations [24] exists for the governing Equation 1-Equation 4 are given below

$$\left\{ u = bx f'(\eta), v = -\sqrt{b\nu} f(\eta), \theta(\eta) = \frac{T - T_\infty}{T_w - T_\infty}, \phi(\eta) = \frac{C - C_\infty}{C_w - C_\infty}, \eta = \sqrt{\frac{b}{\nu}} y. \right\} \tag{7}$$

Here prime denotes differentiation with respect to η. Using Eq. (7) which trivially satisfies the continuity Equation 1, and reduces Equation 2-Equation 4 to the following self-similar equations

$$f''' + f f'' + \lambda f'' f''' - (f')^2 - (Mn + Pt) f' = 0, \tag{8}$$

$$\theta'' + Pr(f\theta' - 2f'\theta) + \frac{Nc}{Le}\theta'\phi' + \frac{Nc}{Nb_t Le}(\theta')^2 + (HgPr)\theta = 0, \tag{9}$$

$$\phi'' + \frac{1}{Nb_t}\theta'' + Scf\phi' - (ScRc)\phi = 0. \tag{10}$$

The pertinent boundary conditions (5)-(6) become

$$\left\{ \begin{array}{c} f(0) = 0, \quad f'(0) = 1 + \xi f''(0), \quad \theta(0) = 1 + \beta\theta'(0), \quad \phi(0) = 1, \\ f'(\infty) \to 0, \quad \theta(\infty) \to 0, \quad \phi(\infty) \to 0, \end{array} \right\} \tag{11}$$

where $\lambda = \sqrt{\frac{2b^3}{\nu}}\Gamma x$ (non-Newtonian Williamson parameter), $Mn = \frac{\sigma B_0^2}{\rho b}$ (Magnetic parameter), $Pt = \frac{\nu}{Kb}$ (porosity parameter) , $Pr = \frac{\nu}{\alpha}$ (Prandtl number), $Nc = \frac{\rho_p C_p (C_w - C_\infty)}{\rho C}$ is the heat capacity ratio parameter which accounts the contribution of nanoparticles in thermal energy storage, $Nb_t = \frac{T_\infty D_B (C_w - C_\infty)}{D_T (T_w - T_\infty)}$ is diffusivity ratio parameter signifies the combined effect of Brownian diffusion and thermophoresis in nanoparticle transport, $Le = \frac{\alpha}{D_B}$ (Lewis number), $Hg = \frac{Q}{b\rho C}$ (heat source/sink parameter), $Sc = \frac{\nu}{D_B}$ (Schmidt number), $Rc = \frac{R}{b}$ (chemical reaction parameter), $\xi = \xi^* \mu \sqrt{\frac{b}{\nu}}$ is the velocity slip parameter and $\beta = \beta^* \sqrt{\frac{b}{\nu}}$ is the thermal slip parameter.

The interesting dimensionless physical parameters viz. Skin friction coefficient C_{f_x}, Local Nusselt number Nu_x and Sherwood number Sh_x are given below

$$\left\{ \begin{array}{c} C_{f_x} = \dfrac{\mu}{\rho U_w^2} \left[\dfrac{\partial u}{\partial y} + \dfrac{\Gamma}{\sqrt{2}} \left(\dfrac{\partial u}{\partial y} \right)^2 \right]_{y=0} = (Re_x)^{-1/2} \left[1 + \dfrac{\lambda}{2} f''(0) \right] f''(0), \\ Nu_x = \dfrac{-kx}{k(T_w - T_\infty)} \left(\dfrac{\partial T}{\partial y} \right)_{y=0} = -(Re_x)^{1/2} \theta'(0), \\ Sh_x = \dfrac{-x}{(C_w - C_\infty)} \left(\dfrac{\partial C}{\partial y} \right)_{y=0} = -(Re_x)^{1/2} \phi'(0). \end{array} \right\} \tag{12}$$

Here, $Re_x = (b/\nu)x^2$ is the local Reynolds number.

TABLE 1. Numerical Comparison for $-\theta'(0)$ varying Prandtl's number with $Le \to \infty$, $Nb_t \to \infty$, $\xi = \beta = \lambda = Mn = Pt = Hg = Rc = Nc = Sc = 0$.

Pr	Zeeshan and Majeed [38]		Grubka and Bobba [20]	Present work	
	RK method	OHAM	Series solution	KBM	HWCM
0.72	1.08853	1.08853	1.0885	1.08853	1.08848
1	1.33333	1.33334	1.3333	1.33333	1.33323
3	2.50972	2.50972	2.5097	2.50972	2.50931
7	-	-	-	3.97151	3.97143
10	4.79687	4.79687	4.7969	4.79687	4.79614
100	-	-	15.7120	15.71204	15.71377

TABLE 2. Numerical comparison of $f''(0)$ varying slip parameter with $\beta = 1$, $\lambda = 0.5$, $Pr = 7$,$Mn = Pt = Rc = Hg = 0$, $Nc = 2.5$, $Nb_t = 2$, $Le = 10$, $Sc = 5$.

	Kho et al. [39]	Present work	
ξ	Shooting method	KBM	HWCM
0.25	-0.824627	-0.824627	-0.824225
0.5	-	-0.633138	-0.632798
0.75	-0.521313	-0.521314	-0.521006
1.0	-	-0.446071	-0.445785
1.25	-0.391317	-0.391317	-0.391048
1.5	-	-0.349397	-0.349142
1.75	-0.316124	-0.316124	-0.315880

3. METHOD OF SOLUTION

It is quite challenging to determine the closed-form solution of coupled non-linear ODEs (8) - (10) with mixed boundary conditions (11) through analytical methods. Thus, numerical and semi-numerical strategies are used to determine the solutions of the flow problem through Keller box and Haar wavelet collocation methods.

3.1. **Keller box method (KBM).** KBM is one of the most elegant and fast converging numerical techniques for solving nonlinear boundary value problems involving intricate geometries. KBM [29] is an implicit finite difference iterative scheme advanced by Newton's quasi-linearisation technique. KBM consists of discretising the domain into mesh points and proceeds iteratively to solve the unknown values at each mesh points. Cebeci and Bradshaw [40] and Na [41] outlined the elaborative steps involved in the KBM for solving various types of problems, emphasizing its accuracy, especially in handling parabolic problems. The principal steps used to solve system of ODEs (8) - (10) with pertinent boundary constraints (11) are as follows

i) The system of higher order differential equations is transformed into system of first order ODEs.
ii) The dependant variables and their derivatives are replaced by corresponding average and finite difference formulas respectively to obtain the nonlinear system of algebraic equations.
iii) The system of non-linear equations are converted into a system of quasi-linear algebraic equations by using Newton's quasi-linearisation technique.
iv) Block tri-diagonal elimination technique is used to solve the algebraic quasi-linear system of equations.

The convergence of Keller-box method is significantly depends on the initial approximations, which must satisfy the boundary conditions of the problem. In the present study results are obtained using a step size $h = 0.001$ adhering to the error tolerance of 10^{-5} which ensures that most of the results are correct up to four decimal places.

3.2. **Haar wavelet collocation method (HWCM).** The integration domain $[A, B]$ of the problem is descritized into $2M$ subintervals of equal length $\Delta\eta = \frac{B-A}{2M}$. According to Lepik [34], the Haar wavelet

TABLE 3. Computation of results for Local Skin friction, Nusselt number and Sherwood number respectively with $Le = 10$,$Sc = 5$, $Mn = 0.5$, $Pt = 0.5$, $Hg = 0.5$, $Rc = 0.5$ and $\eta_\infty \geq 7$

						$-f''(0)$		$-\theta'(0)$		$-\phi'(0)$	
ξ	β	λ	Pr	Nc	Nb_t	KBM	HWCM	KBM	HWCM	KBM	HWCM
1.75	1	0.5	7	2.5	2	0.39013	0.39013	0.58867	0.58867	1.62677	1.62676
1.25						0.49310	0.49310	0.62554	0.62553	1.64163	1.64162
1.0						0.57022	0.57022	0.65103	0.65102	1.65664	1.65664
0.75						0.67945	0.67944	0.67469	0.67469	1.67750	1.67750
0.5						0.85005	0.85004	0.69941	0.69940	1.70863	1.70864
	0.2							1.57732	1.57726	1.45101	1.45105
	0.4							1.20168	1.20164	1.56100	1.56103
	0.6							0.96988	0.96985	1.62906	1.62908
	0.8							0.81281	0.81279	1.67524	1.67527
	1	0				0.77658	0.77658	0.71303	0.71302	1.73399	1.73401
		0.5				0.85005	0.85004	0.69941	0.69940	1.70863	1.70864
		0.75				0.91215	0.91211	0.68711	0.68709	1.69062	1.69064
		1				1.04645	1.04535	0.66014	0.66015	1.66260	1.66263
		0.5	4			0.85005	0.85004	0.61447	0.61446	1.75404	1.75406
			6					0.67813	0.67812	1.72140	1.72142
			8					0.71681	0.71680	1.69755	1.69756
			10					0.74389	0.74388	1.67914	1.67916
			7	15				0.60210	0.60209	1.77419	1.77420
				10				0.64214	0.64213	1.74839	1.74840
				5				0.68091	0.68090	1.72184	1.72186
				2.5	2			0.69941	0.69940	1.70863	1.70864
					1.5			0.69887	0.69886	1.64024	1.64026
					1			0.69779	0.69777	1.50418	1.50421
					0.5			0.69449	0.69447	1.10182	1.10187

functions are defined as

$$h_i(\eta) = \begin{cases} 1, & \text{for } \eta \in [A_1(i), A_2(i)), \\ -1, & \text{for } \eta \in [A_2(i), A_3(i)), \\ 0, & \text{elsewhere,} \end{cases} \tag{13}$$

where

$$A_1(i) = A + 2k\mu\Delta\eta, A_2(i) = A + (2k+1)\mu\Delta\eta, A_3(i) = A + 2(k+1)\mu\Delta\eta, \tag{14}$$

for $k = 0, 1, 2, 3, \ldots, m-1$ and $j = 0, 1, 2, 3, \ldots, J$ represents parameters of translation and dilation respectively. Index i is given as $i = k + m + 1$, the parameter $m = 2^j$ (i.e., $M = 2^J$) is the highest number of sequentially utilized square waves in $[A, B]$ and k stands for specific square wave. The scaling Haar wavelet function for $i = 1$ can be stated as

$$h_i(\eta) = \begin{cases} 1, & \text{if } \eta \in [A, B], \\ 0, & \text{otherwise.} \end{cases} \tag{15}$$

For any square integrable and bounded function $f(x)$ in the interval $[A, B]$ superimposed into Haar wavelet as

$$f(x) = \sum_{i=1}^{\infty} a_i h_i(x), \tag{16}$$

TABLE 4. Computation of results for Local Skin friction, Nusselt number and Sherwood number respectively with $\xi = 0.5, \beta = 0.5$, $\lambda = 0.5$, $Pr = 7$, $Nc = 2.5$, $Nb_t = 2$ and $\eta_\infty \geq 7$

						$-f''(0)$		$-\theta'(0)$		$-\phi'(0)$	
Le	Sc	Mn	Pt	Hg	Rc	KBM	HWCM	KBM	HWCM	KBM	HWCM
1	5	0.5	0.5	0.2	0.6	0.85005	0.85004	0.68379	0.68377	1.93515	1.93515
2								0.88533	0.88531	1.84016	1.84017
5								1.20477	1.20475	1.76539	1.76541
10								1.07174	1.07171	1.73879	1.73881
	8							1.06401	1.06399	2.33951	2.33952
	6							1.06880	1.06877	1.95585	1.95586
	4							1.07522	1.07519	1.49872	1.49783
	2	0.5						1.08509	1.08506	0.89544	0.89547
		1				0.92246	0.92243	1.04096	1.04093	0.89520	0.89522
		1.5				0.98162	0.98159	1.03125	1.03122	0.89898	0.89899
		2				1.03134	1.03129	0.95174	0.95174	0.90614	0.90617
		0.5	0			0.75783	0.75782	1.12872	1.12870	0.90173	0.90173
			1			0.92246	0.92243	1.04096	1.04093	0.89820	0.89522
			1.5			0.98162	0.98159	1.03125	1.03122	0.89898	0.89899
			2			1.03134	1.03129	0.95174	0.95174	0.90614	0.90617
			0.5	0.2		0.85005	0.85004	1.08509	1.08506	0.89544	0.89547
				0.1				1.11704	1.11701	0.87805	0.87808
				0				1.14434	1.14431	0.86272	0.86275
				-0.25				1.19955	1.19950	0.83069	0.83072
				-0.5	0.6			1.24272	1.24267	0.80481	0.80484
					0.4			1.24531	1.24526	0.60693	0.60696
					0.2			1.24868	1.24863	0.36288	0.36292
					0.0			1.25393	1.25387	0.00891	0.00894

where Haar wavelet coefficients a_i's are written as

$$a_i = 2^j \int_A^B h_i(x) f(x) dx, \qquad i = 1, 2, 3, ..., 2^j + k + 1. \tag{17}$$

These a_i's are derived from the minimum threshold condition of integral square error i.e.

$$\int_A^B E_H^2 dx \to \text{minimum} \tag{18}$$

and $|E_H| = |f(x) - f_H(x)|$, $f_H(x) = \sum_{i=0}^{2M} a_i h_i(x)$ where $f(x)$ and $f_H(x)$ are exact and approximate solutions respectively. The n^{th} order integral of Haar functions of Equation 13 is computed analytically as

$$P_{n,i} = \underbrace{\int_A^\eta \int_A^\eta ..... \int_A^\eta}_{n \text{ times}} h_i(x) dx^n = \frac{1}{(n-1)!} \int_A^\eta (t-x)^{n-1} h_i(x) dx, \tag{19}$$

where $i = 1, 2, 3, ..., 2M$ and $n = 1, 2, 3, ..., N$. This corresponds to a function $h_i(\eta)$ for $n = 0$ and using the definition, this integral can be estimated as

$$P_{n,i}(\eta) = \begin{cases} 0, & \text{for } \eta \in [A, A_1(i)), \\ \frac{1}{n!}[\eta - A_1(i)]^n, & \text{for } \eta \in [A_1(i), A_2(i)), \\ \frac{1}{n!}\{[\eta - A_1(i)]^n - 2[\eta - A_2(i)]^n\}, & \text{for } \eta \in [A_2(i), A_3(i)), \\ \frac{1}{n!}\{[\eta - A_1(i)]^n - 2[\eta - A_2(i)]^n + [\eta - A_3(i)]^n\}, & \text{for } \eta \in [A_3(i), B]. \end{cases} \tag{20}$$

Here $i = 1$ shows $A_1 = A$, $A_2 = A_3 = B$ and $P_{n,1}(\eta) = \frac{1}{n!}[\eta - A]^n$. Thus, the formula (20) holds for $i > 1$. $\eta_l = \frac{\eta'_l + \eta'_{l-1}}{2}$ are the collocation points with $l = 1, 2, 3, ...2M$ such that $\eta'_l = A + l\Delta\eta$ denotes l^{th} grid point.

3.2.1. *Solution methodology of Haar wavelet collocation method.* The highest order derivatives present in the system of Equation 8 - Equation 10 are given by

$$f'''(\eta) = \sum_{i}^{2M} a_i h_i(\eta), \quad \theta''(\eta) = \sum_{i}^{2M} b_i h_i(\eta), \quad \phi''(\eta) = \sum_{i}^{2M} c_i h_i(\eta). \tag{21}$$

where a_i, b_i and c_i are Haar wavelet coefficients. Successively integrating Equation 21 to obtain lower order derivatives by utilizing boundary conditions (11). Further, letting $\eta_\infty = \beta'$ and $C'_i = \int_A^{\beta'} P_i(t)dt$ we have

$$\left\{ \begin{array}{c} f''(0) = \dfrac{-1}{\xi + \beta'} \left(1 + \sum_{i=1}^{2M} a_i C'_i \right), \quad \theta'(0) = \dfrac{-1}{\beta + \beta'} \left(1 + \sum_{i=1}^{2M} b_i C'_i \right), \\ \phi'(0) = \dfrac{-1}{\beta'} \left(1 + \sum_{i=1}^{2M} c_i C'_i \right). \end{array} \right\} \tag{22}$$

Using Equation 21 and Equation 22, system of Equation 8 - Equation 10 can be written as

$$\begin{aligned} &\sum_{i=1}^{2M} a_i H_i^l + \left\{ \eta_l \left[1 + \left(\xi + \frac{\eta_l}{2} \right) \frac{-1}{\xi + \beta'} \left(1 + \sum_{i=1}^{2M} a_i C \right) \right] + \sum_{i=1}^{2M} a_i R_i^l \right\} \\ &\left\{ \frac{-1}{\xi + \beta'} \left(1 + \sum_{i=1}^{2M} a_i C \right) + \sum_{i=1}^{2M} a_i P_i^l \right\} + \lambda \left\{ \frac{-1}{\xi + \beta'} \left(1 + \sum_{i=1}^{2M} a_i C \right) + \sum_{i=1}^{2M} a_i P_i^l \right\} \\ &\times \sum_{i=1}^{2M} a_i H_i^l - \left\{ 1 + (\xi + \eta_l) \left\{ \frac{-1}{\xi + \beta'} \left(1 + \sum_{i=1}^{2M} a_i C \right) \right] + \sum_{i=1}^{2M} a_i R_i^l \right\}^2 \\ &-(Mn + Pt) \left\{ 1 + (\xi + \eta_l) \left[\frac{-1}{\xi + \beta'} \left(1 + \sum_{i=1}^{2M} a_i C \right) \right] + \sum_{i=1}^{2M} a_i Q_i^l \right\} = 0, \end{aligned} \tag{23}$$

$$\sum_{i=1}^{2M} b_i H_i^l + Pr\left\{\eta_l\left[1+\left(\xi+\frac{\eta_l}{2}\right)\frac{-1}{\xi+\beta'}\left(1+\sum_{i=1}^{2M} a_i C\right)\right]+\sum_{i=1}^{2M} a_i R_i^l\right\}$$
$$\times\left\{\frac{-1}{\beta+\beta'}\left(1+\sum_{i=1}^{2M} b_i C\right)+\sum_{i=1}^{2M} b_i P_i^l\right\}-2Pr\left\{1+(\xi+\eta_l)\left[\frac{-1}{\xi+\beta'}\left(1+\sum_{i=1}^{2M} a_i C\right)\right]\right.$$
$$\left.+\sum_{i=1}^{2M} a_i Q_i^l\right\}\times\left\{1+(\beta+\eta_l)\left[\frac{-1}{\beta+\beta'}\left(1+\sum_{i=1}^{2M} b_i C\right)\right]+\sum_{i=1}^{2M} b_i Q_i^l\right\}$$
$$+\frac{Nc}{Le}\left\{\frac{-1}{\beta+\beta'}\left(1+\sum_{i=1}^{2M} b_i C\right)+\sum_{i=1}^{2M} b_i P_i^l\right\}\left\{\frac{-1}{\beta'}\left(1+\sum_{i=1}^{2M} c_i C\right)+\sum_{i=1}^{2M} c_i P_i^l\right\}$$
$$+\frac{Nc}{Nb_t Le}\left\{\frac{-1}{\beta+\beta'}\left(1+\sum_{i=1}^{2M} b_i C\right)+\sum_{i=1}^{2M} b_i P_i^l\right\}^2$$
$$+HgPr\left\{1+(\beta+\eta_l)\left[\frac{-1}{\beta+\beta'}\left(1+\sum_{i=1}^{2M} b_i C\right)\right]+\sum_{i=1}^{2M} b_i Q_i^l\right\}=0, \tag{24}$$

$$\sum_{i=1}^{2M} c_i H_i^l+\frac{1}{Nb_t}\sum_{i=1}^{2M} b_i H_i^l+Sc\left\{\eta_l\left[1+\left(\xi+\frac{\eta_l}{2}\right)\frac{-1}{\xi+\beta'}\left(1+\sum_{i=1}^{2M} a_i C\right)\right]+\sum_{i=1}^{2M} a_i R_i^l\right\}$$
$$\times\left\{\frac{-1}{\beta'}\left(1+\sum_{i=1}^{2M} c_i C\right)+\sum_{i=1}^{2M} c_i P_i^l\right\}-ScRc\left\{1-\frac{\eta_l}{\beta'}\left(1+\sum_{i=1}^{2M} c_i C\right)+\sum_{i=1}^{2M} c_i Q_i^l\right\}=0. \tag{25}$$

where $l=1,2,3,\ldots,2M$. $H_i^l=h_i(\eta_l)$, $P_i^l=P_i(\eta_l)$, $Q_i^l=Q_i(\eta_l)$ and $R_i^l=R_i(\eta_l)$ are the square matrices of order $2M\times 2M$ and $C=C_i^l$ is a column vector with $2M$ elements. Typically, Haar and its integral matrices exhibit sparsity.

4. Result and Discussion

The system of nonlinear coupled ODEs (8) - (10) with boundary constraints Equation 11 was solved by using the Keller box and Haar wavelet collocation methods. Table 1 illustrate the validation of the study as $-\theta'(0)$ values obtained using KBM and HWCM exhibit strong numerical agreement with Runge Kutta method [38], optical homotopy analysis method (OHAM) [38] and series method [20]. Further, the obtained values of $f''(0)$ are compared with the shooting method presented in Table 2, which gives an excellent numerical consistency with Kho et al. [39]. The influence of various physical parameters on $-f''(0)$, $-\theta'(0)$ and $-\phi'(0)$ is featured in Table 3 and Table 4. The rise in the Williamson parameter leads to a decrease in the skin friction coefficient. Thus, it can be used as a lubricant in cooling systems, which is beneficial because the suspended nanoparticles remain in the base fluids for a longer time and also improve the flow characteristics of the nanofluid. Moreover, an increase in the Williamson parameter decreases both Nusselt and Sherwood numbers, decelerating the heat and mass transfer efficiency at the surface.

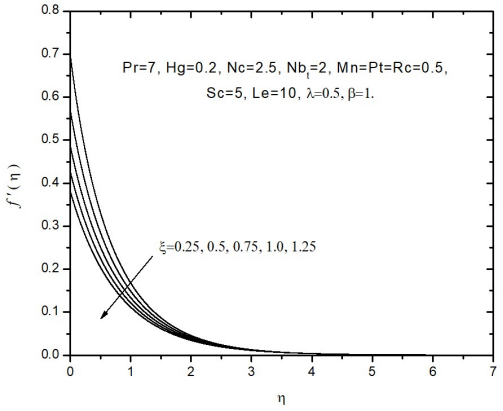

FIGURE 2. Impact of ξ on $f'(\eta)$

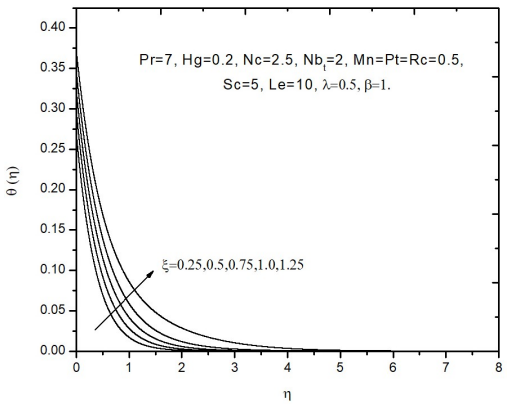

FIGURE 3. Impact of ξ on $\theta(\eta)$

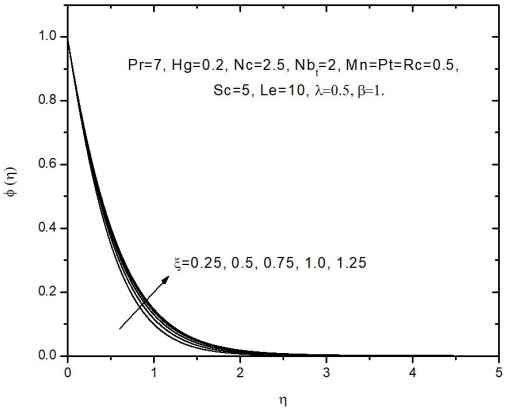

FIGURE 4. Impact of ξ on $\phi(\eta)$

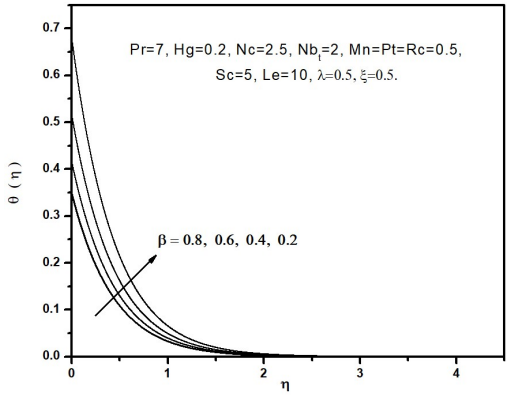

FIGURE 5. Impact of β on $\theta(\eta)$

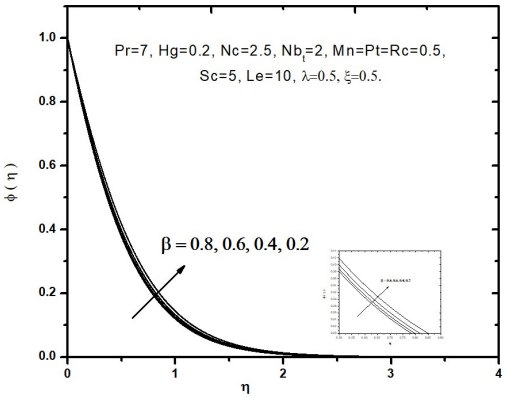

FIGURE 6. Impact of β on $\phi(\eta)$

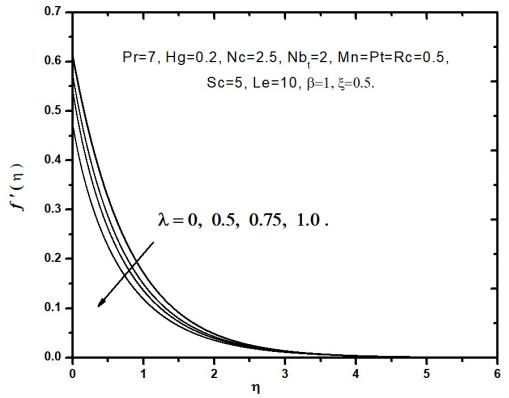

FIGURE 7. Impact of λ on $f'(\eta)$

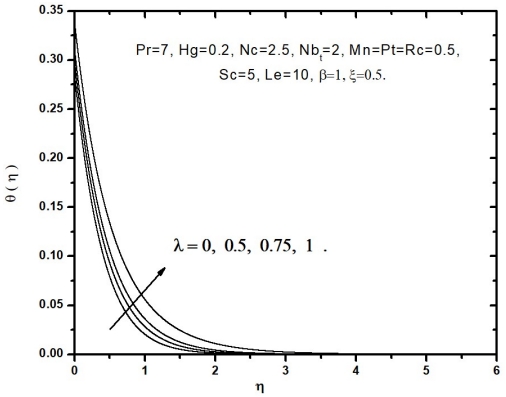

FIGURE 8. Impact of λ on $\theta(\eta)$

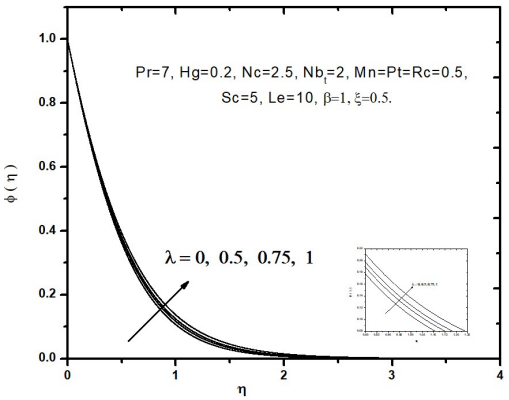

FIGURE 9. Impact of λ on $\phi(\eta)$

Figure 2-4 demonstrate the impact of velocity slip parameter ξ on velocity, temperature and concentration profiles respectively. It is noticed that both the velocity and temperature profiles reduces with increasing values of ξ, whereas nanoparticle volume fraction increases with greater ξ. Figure 5,6 depict the effect of thermal slip parameter on temperature and concentration profiles. Both profiles are enhanced due to the reduction in the thermal slip parameter. However, temperature variations are more significant as compared to the concentration.

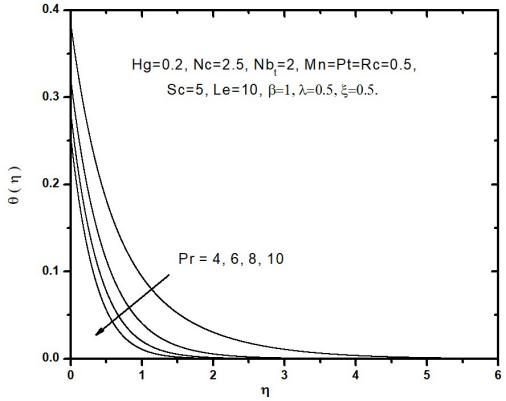

FIGURE 10. Impact of Pr on $\theta(\eta)$

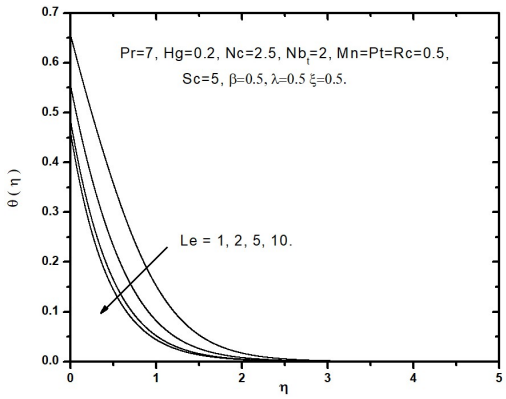

FIGURE 11. Impact of Le on $\theta(\eta)$

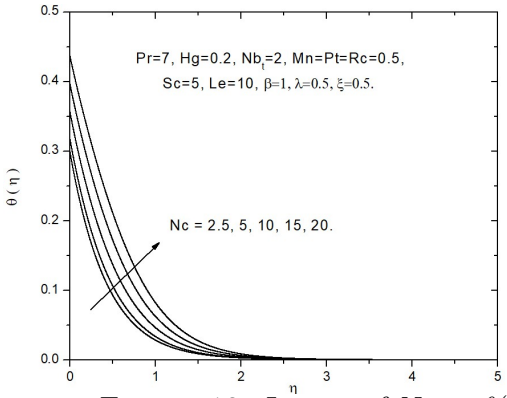

FIGURE 12. Impact of Nc on $\theta(\eta)$

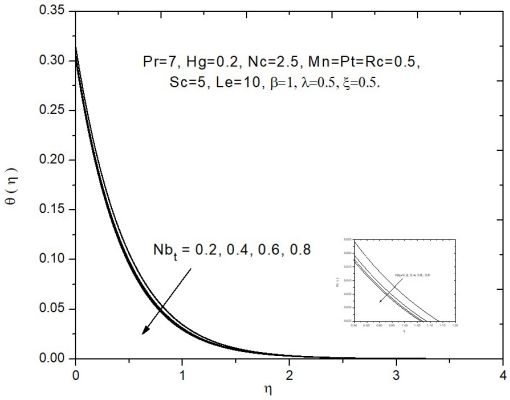

FIGURE 13. Impact of Nb_t on $\theta(\eta)$

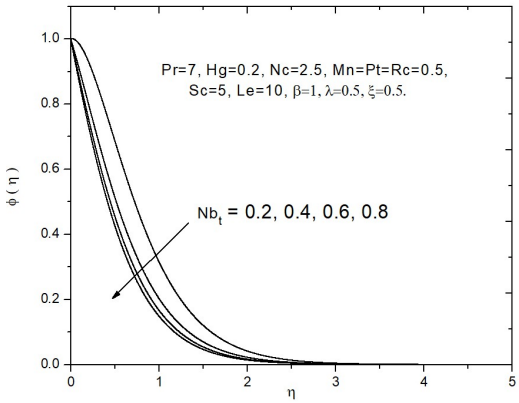

FIGURE 14. Impact of Nb_t on $\phi(\eta)$

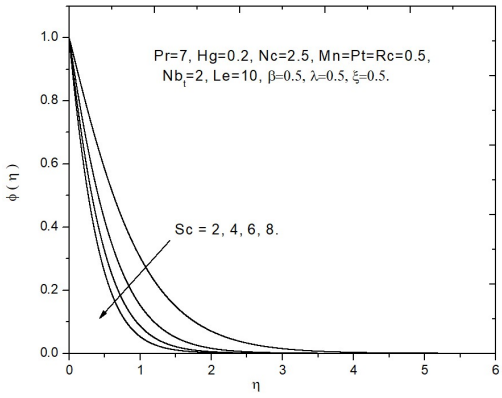

FIGURE 15. Impact of Sc on $\phi(\eta)$

The effect of Williamson parameter on velocity, temperature and concentration profiles is revealed in Figure 7-9. It shows the rise in non-Newtonian Williamson parameter leads to an enhancement of the temperature and concentration distributions while decreasing the velocity profiles. Figure 10 display a decrease in the temperature profiles due to the higher Prandtl number. This is attributed to the fact that, fluids with high Prandtl number exhibit high accuracy and low thermal conductivity. The effect of Lewis number on temperature profiles are displayed in Figure 11. It demonstrate that, higher Lewis

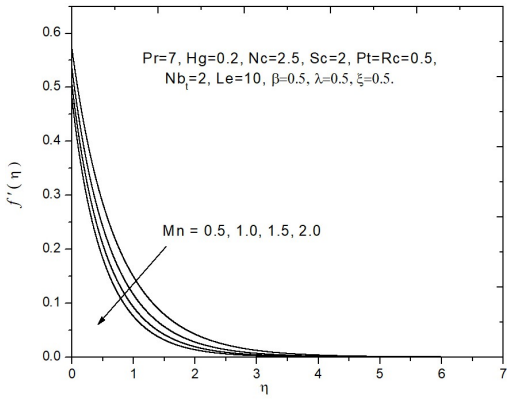

FIGURE 16. Impact of Mn on $f'(\eta)$

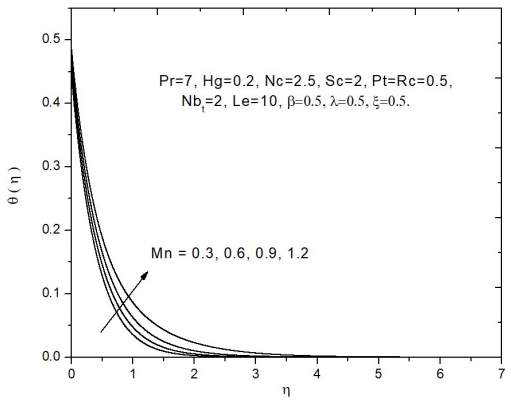

FIGURE 17. Impact of Mn on $\theta(\eta)$

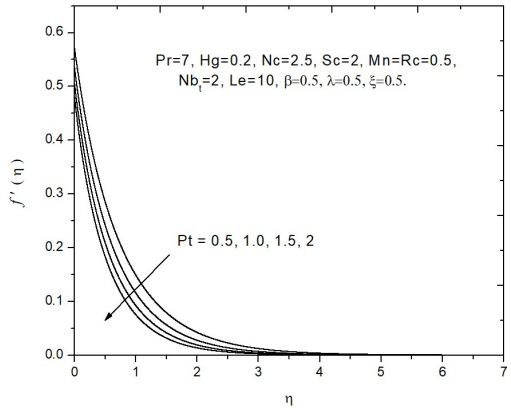

FIGURE 18. Impact of Pt on $f'(\eta)$

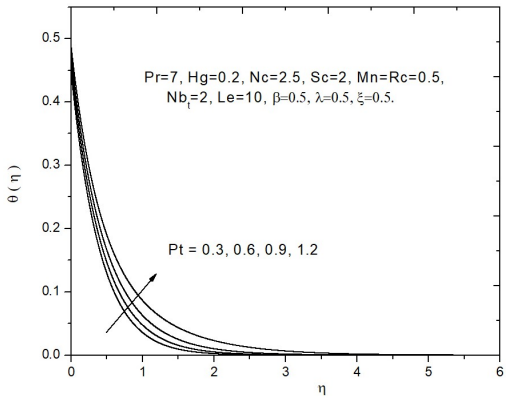

FIGURE 19. Impact of Pt on $\theta(\eta)$

number results in a thinner thermal boundary layer. Since thermal diffusivity is relatively increased as compared to mass diffusivity. The impact of heat capacity ratio parameter on temperature profiles is depicted in Figure 12. It is evident that, temperature profiles increase significantly as heat capacity ratio parameter improves. Figure 13-14 illustrate the effect of diffusivity ratio parameter N_{bt} on temperature and concentration profiles respectively. Both temperature and concentration profiles diminishes with increasing value of N_{bt} , but notable variations are noticed in concentration profiles as compared to temperature. Figure 15 present the concentration profiles for different Schmidt number. It is seen that, concentration profiles decrease remarkably for increasing the Schmidt number, which causes due to the increase in momentum diffusivity and reduces mass transfer rate. Figure 16,17 demonstrate the effect of magnetic parameter on velocity and temperature profiles. It shows the velocity profiles decreases whereas temperature profiles increases with increasing values of magnetic parameter. Temperature increases due to magnetic field induces joule heating within the fluid and velocity decreases as a result of the Lorentz force induced by magnetic field. Figure 18,19 exhibit the porosity effects on velocity and temperature profiles. The velocity profiles decreases and heat transfer increases with enhancing the porosity of the medium. Figure 20 depict the concentration profiles against chemical reaction parameter. It reveals that, nanoparticle volume fraction reduces with increase in chemical reaction parameter. From Table 4, it is evident that, increase in heat generation parameter leads to minimizing the local Nusselt number and augmenting the local Sherwood number. On the other hand, increase in heat absorption parameter leads to increase the local Nusselt number and decrease the local Sherwood number.

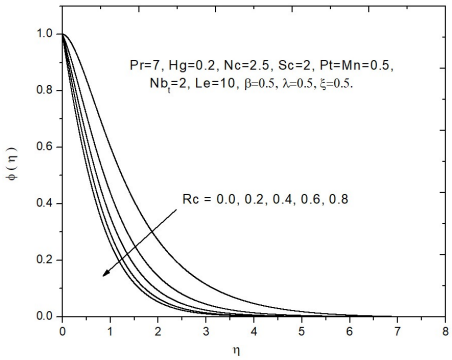

FIGURE 20. Impact of Rc on $\phi(\eta)$.

5. Conclusion

The present study explored the mixed convective MHD Williamson nanofluid flow over a permeable stretching surface, incorporating various thermophysical parameters on heat and mass transfer. The above investigation summarizes the following keynote conclusions

(1) The proposed KBM and HWCM approaches ensured high accuracy with an efficient convergence rate in fewer iterations.
(2) An increase in the non-Newtonian Williamson parameter enhances both temperature and concentration profiles of the nanofluid, while declining the velocity as well as skin friction coefficient of Williamson nanofluid.
(3) The rise in velocity slip parameter improves heat and mass transfer efficiency but decelerates the nanofluid velocity.
(4) A decrease in the thermal slip parameter intensifies temperature and concentration profiles of the Williamson nanofluid. In contrast, an increase in diffusivity ratio parameter reduces the heat and mass transfer.
(5) An increase in Lewis and Prandtl numbers reduces the temperature distribution. Though temperature increases with increasing heat capacity ratio parameter.
(6) Increasing values of Mn and Pt decelerates the velocity but accelerates the heat transfer. Moreover, nanoparticle volume fraction decreases due to increasing Schmidt number and chemical reaction parameter.
(7) An increase in the heat generation/absorption parameter yields a decrease in the Nusselt number and an increase in the Sherwood number.

Declaration

The authors declare that there is no conflict of interest regarding the publication of this paper

Financial Support

The authors received no specific funding for this work.

References

1. Choi, S.U.S., *Enhancing thermal conductivity of fluids with nanoparticle.* in:D. A. Siginer and H. P. Wang (Eds.), Developments and Applications of non- Newtonian flows, ASME, New York **66** (1995), 99-105.
2. Eastman, J.A., Choi, S.U.S., Li, S., Yu, W., and Thompson, L.J., *Enhanced thermal conductivity through the developement of nanofluids*, Mater. Res. Soc. Symp. Proc., vol. 457 , 1997, pp. 3-11.
3. Taylor, R., Sylvain, C., Todd, O., Phelan, P., and Gunawan, A., *Small particles, big impacts: A review of the diverse applications of nanofluids.* J. Appl. Phys. **113** (2013), 011301.
4. Buongiorno, J., *Convective transport in nanofluids.* J. Heat Transf. **128(3)** (2005), 240-250.
5. Corcione, M., Cianfrini, M., and Quintino, A., *Two-phase mixture modelling of natural convection of nanofluids with temperature-dependent properties.* Int. J. Therm. Sci. **71** (2013), 182-195.

6. Rana, P., and Bhargava, R., *Flow and heat transfer of a nanofluid over a nonlinearly stretching sheet.* Common. Nonlinear Sci. Numer. Simul. **17** (2012), 212-226.
7. Xuan, Y., and Li, Q., *Investigation on convective heat transfer and flow features of nanofluids.* J. Heat Transf. **9(2)** (2016), 729-739.
8. Wong, K.V., and Leon, O.D., *Review article: Applications of nanofluids; current and future.* Adv. Mech. Engg. **20** (2010), 519659.
9. Krishnamurthy, M.R.,Gireesha, B.J., Prasannakumara, B.C., and Gorla, R.S.R., *Thermal radiation and chemical reaction effects on boundary layer slip flow and melting heat transfer of nanofluid induced by a nonlinear stretching sheet.* Nonlinear Engg. **5** (2016), 147-159.
10. Blasius, H., *The boundary layers in fluids with little friction* Natl. Advis. Comm. Aeronaut., 1950.
11. Ramesh, G.K., Gireesha, B.J., and Gorla, R.S.R., *Study on Sakiadis and Blasius flows of Williamson fluid with convective boundary condition.* Nonlinear. Engg. **4(4)** (2015), 215-221.
12. Awati, V.B., Maheshkumar, N., and Wakif, A., *Haar wavelet scrutinization of heat and mass transfer features during the convective boundary layer flow of a nanofluid moving over a nonlinearly stretching sheet.* Partial Diff. Eq. Appl. Math.**4** (2021), 100192.
13. Awati, V.B., and Maheshkumar, N., *Analysis of forced convection boundary layer flow and heat transfer past a semi-infinite static and moving flat plate using nanofluids by Haar wavelets.* J. Nanpfluids **10** (2021), 106-117.
14. Liao, S., *A new branch of solutions of boundary-layer flows over an impermeable stretched plate.* Int. J. Heat Mass Transf. **48(12)** (2005), 2529-2539.
15. Khan, N.A., and Khan, H., *A boundary layer flows of non-Newtonian Williamson fluid.* Nonlinear Engg. **3(2)** (2014), 107-115.
16. Crane, L.J., *Flow past a stretching plate.* Zeitschrift für Angewandte Mathematik und Physik (ZAMP) **21** (1970), 645-647.
17. Ishak, A., Nazar, R., and Pop, I., *Hydrodynamic flow and heat transfer adjacent to a stretching vertical sheet.* Heat Mass Transf. **44** (2008), 921-927.
18. Nadeem, S. and Hussain, S.T., *Analysis of MHD Williamson nano fluid flow over a heated surface.* J. Appl. Fluid Mech. **9(2)** (2016), 729-739.
19. Kumar, S.G., Varma, S.V.K., Kirankumar, R.V.M.S.S.,Raju, C.S.K., Shehzad, S.A., and Bashir, M.N., *Three-dimensional hydromagnetic convective flow of chemically reactive Williamson fluid with non-uniform heat absorption and generation.* Int. J. Chem. Reactor Engg. **17** (2018), 118.
20. Grubka, L.G., and Bobba, K.M., *Heat transfer characteristics of a continuous stretching surface with variable temperature.* J. Heat Transf. **107** (1985), 248-250.
21. Chen, C.H., *Laminar mixed convection adjacent to vertical continuously stretching sheets.* Heat Mass Transf. **33** (1998), 471-476.
22. Rosali, H., Ishak, A., and Pop, I., *Micropolar fluid flow towards a stretching/shrinking sheet in a porous medium with suction.* Int. Commun. Heat Mass Transf. **39(6)** (2012), 826-829.
23. Hayat, T., Qasim, M., and Mesloub, S., *MHD flow and heat transfer over permeable stretching sheet with slip conditions.* Int. J. Numer. Meth. Fluids **66(8)** (2011), 963-975.
24. Yasin, M.H., Ishak, A., and Pop, I., *MHD heat and mass transfer flow over a permeable stretching/shrinking sheet with radiation effect.* J. Magn. Mater. **407** (2016), 235-240.
25. Nazir, U., Sadiq, M.A., and Nawaz, M., *Non-Fourier thermal and mass transport in hybrid nano-Williamson fluid under chemical reaction in Forchheimer porous medium.* Int. Commun. Heat and Mass Transf. **127** (2021), 105536.
26. Awati, V.B., Goravar, A., and Maheshkumar, N., *Semi-Numerical investigation of boundary layer flow and heat transfer of Magnetohydrodynamic nanofluid flow in presence of chemical reaction over a non-isothermal porous medium.* ASME J. Heat and Mass Transf. **145(8)** (2023), 084503.
27. Awati, V.B., Goravar, A., Maheshkumar, N., and Chamkha, A.J., *Scrutinization of Chebyshev collocation method for mass transfer on a continuous flat plate moving in parallel to a free stream in the presence of a chemical reaction.* Int. J. Amb. Energy **44(1)** (2022), 390-398.
28. Ramya, D., Srinivasa, R., Rao, J.A. and Chamkha, A.J., *Effects of velocity and thermal wall slip on MHD boundary layer viscous flow and heat transfer of a nanofluid over a nonlinearly stretching sheet.* Propuls. Power Research **7(2)** (2018), 182-195.
29. Vajravelu, K., and Prasad, K.V., *Keller box method and its application* Walter de Gruyter GmbH and Co., 2014, pp. 279-382.
30. Bilal, S., Khalil, U.R., and Malik, M. Y., *Numerical investigation of thermally stratified Williamson fluid flow over a cylindrical surface via Keller box method.* Results Phys. **7** (2017), 690-696.
31. Daubechies, I., *Ten lectures on wavelets* Soc. Indus. Appl. Math. 1992.
32. Grossman, A., and Morlet, J., *Decomposition of Hardy functions into square integrable wavelets of constant shape.* SIAM J. Math. Anal. **15(4)** (1984), 723-736.
33. Chen, C., and Hsiao, C., *Haar wavelet method for solving lumped and distributed parameter systems.* IEE Proc. Control Theory and Applications, 1997, pp. 87-94.

34. Lepik, U., *Numerical solution of differential equations using Haar wavelets.* Math. Comput. Simul. **68(2)** (2005), 127-143.
35. Lepik, U., *Solving integral and differential equations by the aid of non-uniform Haar wavelets.* Appl. Math. Comput. **198(1)** (2008), 326-332.
36. Awati, V.B., Goravar, A., and Maheshkumar, N., *Spectral and Haar wavelet collocation method for the solution of heat generation and viscous dissipation in micro-polar nanofluid for MHD stagnation point flow.* Math. Comput. Simul. **215** (2024), 158-183.
37. Awati, V. B., Muchandi, S.S., Maheshkumar, N., Muhammad, T., Zaydan, M., Wakif, A., and Sehaqui, R., *New insights into transport phenomena within steady MHD two-phase nanofluid fows over a permeable elastic sheet of an uneven thickness.* Modern Phys. Lett. B **39(15)** (2025), 2450488.
38. Zeeshan, A., and Majeed, A., *Heat transfer analysis of Jeffery fluid flow over a stretching sheet with suction/injection and magnetic dipole effect.* Alex. Eng. J. **55(3)** (2016), 2171-2181.
39. Kho, Y.B., Hussanan, A., Mohamed, M.K.A., and Salleh, M.Z., *Heat and mass transfer analysis on flow of Williamson nanofluid with thermal and velocity slips: Buongiorno model.* Propulsion Power Research **8(3)** (2019), 1-10.
40. Cebeci, T., and Bradshaw, P., *Physical and computational aspects of convective heat transfer*, Springer, New York, 2013.
41. Na, T. Y., *Computational methods in engineering boundary value problems*, Academic Press, New York, 1980.